AIAA JOURNAL
Vol. 42, No. 6, June 2004

Multipoint and Multi-Objective Aerodynamic Shape Optimization

Marian Nemec* and David W. Zingg†
University of Toronto, Toronto, Ontario M3H 5T6, Canada
and
Thomas H. Pulliam‡
NASA Ames Research Center, Moffett Field, California 94035

A gradient-based Newton–Krylov algorithm is presented for the aerodynamic shape optimization of single- and multi-element airfoil configurations. The flow is governed by the compressible Navier–Stokes equations in conjunction with a one-equation transport turbulence model. The preconditioned generalized minimal residual method is applied to solve the discrete-adjoint equation, which leads to a fast computation of accurate objective function gradients. Optimization constraints are enforced through a penalty formulation, and the resulting unconstrained problem is solved via a quasi-Newton method. The new algorithm is evaluated for several design examples, including the lift enhancement of a takeoff configuration and a lift-constrained drag minimization at multiple transonic operating points. Furthermore, the new algorithm is used to compute a Pareto front based on competing objectives, and the results are validated using a genetic algorithm. Overall, the new algorithm provides an efficient approach for addressing the issues of complex aerodynamic design.

Introduction

CURRENT algorithms for the solution of the two-dimensional Navier–Stokes equations provide reasonable predictions of aerodynamic performance for complex airfoil geometries.[1] Although still a subject of research, the solvers are becoming accurate, robust, and computationally inexpensive. For the solution of the aerodynamic shape optimization problem, the validated solvers are typically combined with numerical optimization methods, in particular gradient- and nongradient-based methods. Perhaps the most popular approach for the computation of the objective function gradient is the adjoint method[2–7] because its cost is virtually independent of the number of design variables. Nongradient-based methods, such as genetic algorithms,[8–10] are generally not as efficient as gradient-based methods; however, they may be advantageous for complex, nonsmooth, multi-objective problems.

A classic aerodynamic application of numerical optimization methods is the design of cruise configurations for transonic flow[11–13] and recently for supersonic flow.[14,15] Furthermore, the application of these methods to the design of high-lift configurations is also an active area of research.[16–21] An efficient high-lift configuration can significantly improve the aerodynamic performance of an aircraft, as well as provide weight savings and reductions in mechanical complexity.[22] Therefore, to address all aspects of aerodynamic design, a practical algorithm requires effective capabilities for optimization using multiple objectives, which may include multidisciplinary interactions,[23] and multiple operating points.

A well-known approach for solving multipoint and multi-objective problems is the weighted-sum method. Detailed examples of this method for the multipoint design of cruise configurations are provided by Drela.[24] The main shortcoming of this method is the selection of appropriate design points and their associated weights. The profile optimization method recently introduced by Li et al.[25] and the probabilistic approach suggested by Huyse et al.[26] are promising robust design techniques that address this difficulty.

In Ref. 27, we presented an accurate and efficient algorithm for the calculation of the gradient via the discrete-adjoint approach. The adjoint equation is solved using the preconditioned generalized minimal residual (GMRES) Krylov subspace method (see Ref. 28). Furthermore, the same preconditioned GMRES method is also used within a Newton–Krylov flow solver for fast solution of the Navier–Stokes equations. Overall, the gradient is obtained in just one-fifth to one-third of the time required for a flow solution.

The objectives of this paper are to extend and evaluate the Newton–Krylov algorithm presented in Ref. 27 to the following three areas of aerodynamic design: 1) optimization of high-lift configurations, 2) multi-objective optimization, and 3) multipoint optimization. Factors under consideration include efficiency of the optimization, design robustness, global and local minima, and the computation of Pareto fronts. A genetic algorithm, presented in Ref. 10, is used to validate the multi-objective results.

Problem Formulation

The aerodynamic shape optimization problem consists of determining values of design variables $\boldsymbol{X}$, such that the objective function $\mathcal{J}$ is minimized,

$$\min_{X} \mathcal{J}(\boldsymbol{X}, \boldsymbol{Q}) \tag{1}$$

subject to constraint equations C_j,

$$C_j(\boldsymbol{X}, \boldsymbol{Q}) \leq 0, \qquad j = 1, \ldots, N_c \tag{2}$$

where the vector $\boldsymbol{Q}$ denotes the conservative flow variables and N_c denotes the number of constraint equations. The flow variables are forced to satisfy the governing flow equations, $\mathcal{F}$, within a feasible region of the design space Ω,

$$\mathcal{F}(\boldsymbol{X}, \boldsymbol{Q}) = 0, \qquad \forall \quad \boldsymbol{X} \in \Omega \tag{3}$$

which implicitly defines $\boldsymbol{Q} = f(\boldsymbol{X})$.

Received 13 November 2002; revision received 20 October 2003; accepted for publication 9 January 2004.

*Graduate Student, Institute for Aerospace Studies, 4925 Dufferin Street; currently NRC Research Associate, Applications Branch, Advanced Supercomputing Division, NASA Ames Research Center, Moffett Field, CA 94035; nemec@nas.nasa.gov.

†Professor, Institute for Aerospace Studies, 4925 Dufferin Street; dwz@oddjob.utias.utoronto.ca. Senior Member AIAA.

‡Senior Research Scientist, Applications Branch, Advanced Supercomputing Division; tpulliam@mail.arc.nasa.gov. Associate Fellow AIAA.

For the examples under consideration here, the objective function is given by

$$\mathcal{J} = \begin{cases} \omega_L \left(1 - C_L / C_L^*\right)^2 + \omega_D \left(1 - C_D / C_D^*\right)^2 & \text{if} \quad C_D > C_D^* \\ \omega_L \left(1 - C_L / C_L^*\right)^2 & \text{otherwise} \end{cases} \tag{4}$$

where C_D^* and C_L^* represent target drag and lift coefficients, respectively. The weights ω_D and ω_L are user-specified constants. We find this formulation of the objective function particularly useful because it provides an intuitive approach for the selection of weights and additional terms, such as the moment coefficient, can be readily included. The weighted-sum method is used for multipoint optimization problems:

$$\mathcal{J}_m = \sum_{i=1}^{N_m} w_i \mathcal{J}_i \tag{5}$$

where N_m is the number of design points (typically Mach numbers) and w_i a user-assigned weight for each design point.

The design variables are based on a B-spline parameterization[27,29] of the airfoil. An example is shown in Fig. 1, where a B-spline curve is fitted over the upper surface of the main element, and also the upper surface of the flap for the National Aerospace Laboratory (NLR) 7301 configuration.[30] The vertical coordinates of the B-spline control points are used as design variables. Depending on the problem of interest, additional design variables may include the angle of attack and the horizontal and vertical translation associated with each high-lift element in multi-element configurations, labeled as F_x and F_y in Fig. 1. The horizontal and vertical translation design variables control the gap and overlap distances in the slot region of the airfoil, as defined in Fig. 2.

The constraint equations (2) represent airfoil thickness constraints that are used to ensure feasible designs. The constraints are given by

$$h^*(z_j) - h(z_j) \leq 0 \tag{6}$$

where $h^*(z_j)$ is the minimum allowable thickness at location z_j expressed as a fraction of the airfoil's chord. For multi-element

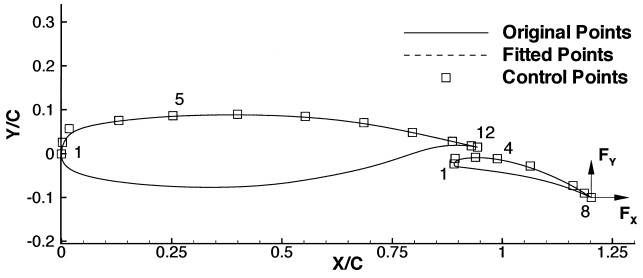

Fig. 1 B-spline curves and flap translation design variables.

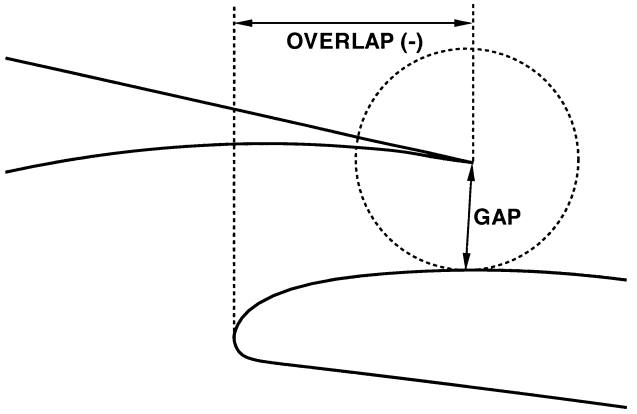

Fig. 2 Definition of gap and overlap distances.

configurations, it is also necessary to constrain the gap and overlap distances. These constraints are required to ensure a reasonable computational grid and are usually inactive at the optimal solution.

The governing flow equations are the compressible two-dimensional thin-layer Navier–Stokes equations in generalized coordinates:

$$\frac{\partial \hat{\boldsymbol{E}}(\boldsymbol{X}, \hat{\boldsymbol{Q}})}{\partial \xi} + \frac{\partial \hat{\boldsymbol{F}}(\boldsymbol{X}, \hat{\boldsymbol{Q}})}{\partial \eta} = Re^{-1} \frac{\partial \hat{\boldsymbol{S}}(\boldsymbol{X}, \hat{\boldsymbol{Q}})}{\partial \eta} \tag{7}$$

where $\hat{\boldsymbol{Q}} = J^{-1}\boldsymbol{Q} = J^{-1}[\rho, \rho u, \rho v, e]^T$ is the vector of conservative dependent state variables, ξ and η are the streamwise and normal generalized coordinates, respectively, and J is the Jacobian of the coordinate transformation from Cartesian coordinates. Vectors $\hat{\boldsymbol{E}}$ and $\hat{\boldsymbol{F}}$ represent the inviscid flux vectors, the viscous flux vector is given by $\hat{\boldsymbol{S}}$, and Re is the Reynolds number. The equations are in nondimensional form. For further details, see Ref. 31. The turbulent viscosity is modelled with the Spalart–Allmaras turbulence model.[32] All cases considered in this study are assumed to be fully turbulent, and therefore the laminar–turbulent trip terms are not used.

Numerical Method

The aerodynamic shape optimization problem defined by Eqs. (1–3) is cast as an unconstrained problem. This is accomplished by lifting the side constraints (2), into the objective function $\mathcal{J}$ using a penalty method. Furthermore, the constraint imposed by the flow equations (3) is satisfied at every point within the feasible design space, and consequently, these equations do not explicitly appear in the formulation of the optimization problem.

The unconstrained problem is solved using the Broyden–Fletcher–Goldfarb–Shanno quasi-Newton method in conjunction with a backtracking line search (see Refs. 27 and 33). At each step of the line search, the objective function value and gradient are required to construct a local cubic interpolant. Note that the optimization problem is based on the discrete form of the flow equations. Using the discrete approach, we expect the gradient to vanish at the optimal solution. In the following sections, we present the formulation for the penalized objective function, as well as the algorithms used for the flow solution, the gradient evaluation, and the grid-perturbation strategy.

Objective with Constraints

A penalty method is used to combine the objective function with the constraint equations. For example, the formulation for the thickness constraints is given by

$$\mathcal{J} = \mathcal{J}_d + \omega_T \sum_{j=1}^{N_c} C_j \tag{8}$$

where $\mathcal{J}_d$ is to the design objective given by Eq. (4), $\mathcal{J}_T$ denotes the thickness penalty terms, and ω_T is a user-specified constant. The penalty terms are based on Eq. (6) and are cast using the following quadratic function:

$$C_j = \begin{cases} \left[1 - h(z_j) / h^*(z_j)\right]^2 & \text{if } h(z_j) < h^*(z_j) \\ 0 & \text{otherwise} \end{cases} \tag{9}$$

A similar formulation is used to enforce the lower and upper bounds for the gap and overlap distances.

Flow Evaluation

The spatial discretization of the flow equations (7) is the same as that used in ARC2D[31] and TORNADO[34] for multiblock H-topology grids. The discretization consists of second-order centered-difference operators with second- and fourth-difference scalar artificial dissipation. The Spalart–Allmaras turbulence model

is discretized as described in Ref. 32 (also see Ref. 35). Overall, the spatial discretization leads to a nonlinear system of equations

$$\boldsymbol{R}(\boldsymbol{X}, \hat{\boldsymbol{Q}}) = 0 \tag{10}$$

where $\hat{\boldsymbol{Q}}$ is the discrete vector of conservative dependent flow variables including the turbulence model variable $\tilde{\nu}$. Hence, at each node (j, k) within the computational domain, $\hat{\boldsymbol{Q}}_{j,k} = (J^{-1}\boldsymbol{Q})_{j,k} = J^{-1}[\rho, \rho u, \rho v, e, \tilde{\nu}]^T_{j,k}$. The turbulence model equation is scaled by J^{-1}. On multiblock grids, the block interfaces are overlapped in the streamwise direction and averaged in the normal direction. Two columns of halo points are used at the streamwise block interfaces. Although $\boldsymbol{R}$ is written as a function of the design variables, we emphasize that during a flow solution the design variables, and consequently the computational grid, are constants.

Equation (10) is solved in a fully coupled manner, where convergence to steady state is achieved using the preconditioned GMRES algorithm in conjunction with an inexact-Newton strategy (see Refs. 27, 36, and 37). The main components include matrix-free GMRES and a block-fill incomplete lower–upper (LU) factorization (BFILU) preconditioner. The matrix–vector products required at each GMRES iteration are formed with first-order finite differences. On the basis of numerical experiments, the number of GMRES search directions is limited to 40 [GMRES(40)], and we do not allow GMRES restarts.[37] Right preconditioning is used, and the preconditioner is based on an approximate flow Jacobian matrix. The level of fill in the BFILU factorization for most cases is two [BFILU(2)], but difficult multi-element cases may require a level of fill of four [BFILU(4)]. The approximate-factorization algorithm of ARC2D in diagonal form[31,34] in conjunction with a subiteration scheme[32] for the turbulence model equation is used to reduce the initial residual by three orders of magnitude to avoid Newton startup problems.

The approximate flow Jacobian matrix used for the preconditioner is identical to the flow Jacobian matrix, $\partial\boldsymbol{R}/\partial\boldsymbol{Q}$, except for the treatment of the artificial-dissipation coefficients.[27] Hence, the preconditioner contains the contributions from all components of the residual vector, namely, inviscid and viscous fluxes, boundary conditions, block interfaces, and the turbulence model. The artificial-dissipation coefficients, which include the spectral radius and the pressure switch, are assumed to be constant with respect to the flow variables. Furthermore, the preconditioning matrix is formed with only second-difference dissipation, but the second-difference coefficient is combined with the fourth-difference coefficient as

$$d_l^{(2)} = d_r^{(2)} + \phi d_r^{(4)} \tag{11}$$

where the subscript r denotes the contribution from the right-hand side and the subscript l denotes the resulting left-hand-side value used in forming the preconditioner. This modification does not affect the steady-state solution. Fast convergence is obtained with the value of ϕ set to 6.0, which has been determined through numerical experiments.

Equation (11) improves the diagonal dominance of the preconditioning matrix and reduces the work and storage requirements of the incomplete factorization. This approach is similar to the "diagonal shift" strategy suggested by Chow and Saad.[38] The present preconditioning matrix is a compromise between a preconditioner based on a first-order upwind discretization of the flow equations and a preconditioner based on the actual second-order discretization. This novel intermediate preconditioner is significantly more effective than either of these more commonly used approaches.

Gradient Evaluation

Using the discrete-adjoint method, the expression for the gradient $\mathcal{G}$ of the objective function $\mathcal{J}[X, \boldsymbol{Q}(\boldsymbol{X})]$ is given by

$$\mathcal{G} = \frac{\mathrm{d}\mathcal{J}}{\mathrm{d}\boldsymbol{X}} = \frac{\partial\mathcal{J}}{\partial\boldsymbol{X}} - \boldsymbol{\psi}^T\frac{\partial\boldsymbol{R}}{\partial\boldsymbol{X}} \tag{12}$$

where we reduce the vector of design variables $\boldsymbol{X}$ to a scalar to clearly distinguish between partial and total derivatives. For problems with multiple design variables, it may be helpful to note that $\mathcal{G}$ and $\partial\mathcal{J}/\partial\boldsymbol{X}$ are $[1 \times N_D]$ row vectors, $\boldsymbol{\psi}$ is a $[N_F \times 1]$ column vector, and $\partial\boldsymbol{R}/\partial\boldsymbol{X}$ is a $[N_F \times N_D]$ matrix, where N_D is the number of design variables and N_F is the number of flow variables. We assume that the implicit function $\boldsymbol{Q}(\boldsymbol{X})$ defined by Eq. (10) is sufficiently smooth even in the presence of flow discontinuities such as shock waves.[39–41]

The vector $\boldsymbol{\psi}$ represents adjoint variables, which are given by the adjoint equation

$$\frac{\partial\boldsymbol{R}}{\partial\boldsymbol{Q}}^T\boldsymbol{\psi} = \frac{\partial\mathcal{J}}{\partial\boldsymbol{Q}}^T \tag{13}$$

This is a large, sparse, linear system of equations that is independent of the design variables. The GMRES strategy from the flow solver is adopted to solve the adjoint equation. Fast solutions are obtained with GMRES(85), and for the preconditioning matrix we use BFILU(6) and $\phi = 3.0$. Multi-element airfoil cases with complex flowfields may require $\phi = 6.0$, which improves the robustness of the adjoint solver. Because of the transpose on the left-hand side of Eq. (13), the matrix-free approach used in the flow solver is not possible for the adjoint equation. The flow Jacobian matrix is stored explicitly, where we include the contribution from the spectral radius, but we treat the pressure switch associated with the artificial-dissipation scheme as a constant.

The remaining terms in Eqs. (12) and (13), namely, the objective function sensitivities $\partial\mathcal{J}/\partial\boldsymbol{X}$ and $\partial\mathcal{J}/\partial\boldsymbol{Q}$, as well as the residual sensitivity $\partial\boldsymbol{R}/\partial\boldsymbol{X}$, are evaluated using centered differences. The use of centered differences for the evaluation of the partial derivative terms is not computationally expensive. For example, the centered-difference formula for the residual sensitivities is given by

$$\frac{\partial\boldsymbol{R}}{\partial\boldsymbol{X}_i} = \frac{\boldsymbol{R}(\boldsymbol{X} + h\boldsymbol{e}_i, \boldsymbol{Q}) - \boldsymbol{R}(\boldsymbol{X} - h\boldsymbol{e}_i, \boldsymbol{Q})}{2h} \tag{14}$$

where

$$h = \max\left(\epsilon \cdot |X_i|, 1 \times 10^{-8}\right) \tag{15}$$

and $i = 1, \ldots, N_D$. The ith unit vector is $\boldsymbol{e}_i$, and a typical value of ϵ is 1×10^{-5}. Note that Eq. (14) involves two evaluations of only the residual vector per design variable and not two flow solutions. Furthermore, the evaluation of residual sensitivities includes the evaluation of grid sensitivities because the design variables do not explicitly appear in the residual equations except for the angle-of-attack design variable.

Grid-Movement Strategy

As the shape and position of an airfoil evolve during the optimization process, the location of the grid nodes is adjusted from the baseline configuration to conform to the new configuration. In Ref. 27, we use an algebraic grid-perturbation strategy that preserves the distance to the outer boundary and relocates the grid nodes in the normal direction proportional to the distance from the airfoil boundary. When the optimization problem involves the horizontal and vertical translation of a slat or a flap, the use of this strategy can result in significantly skewed grid cells near the boundary.[37]

To improve the quality of the modified multiblock grids, we present a new grid-perturbation strategy given by

$$y_k^{\text{new}} = y_k^{\text{old}} + (\Delta y/2)[1 + \cos(\pi S_k)] \tag{16}$$

where Δy is the airfoil shape change. S_k is the normalized arclength distance given by

$$S_k = \frac{1}{L_g}\sum_{i=2}^{k} L_i, \qquad k = 2, \ldots, k_{\max} - 1 \tag{17}$$

where $S_1 = 0$, L_i is the length of a segment between nodes k and $k-1$, and L_g is the grid-line length from the body to the outer boundary.

Results and Discussion

Before presenting aerodynamic design examples, we carefully validate the performance of the flow solver and the gradient computation algorithm. C-topology grids for single-element configurations consist of 257×57 nodes, where the distance to the outer boundary is 24 chords (c), the off-wall spacing is $2 \times 10^{-6}c$, the leading-edge clustering is $5 \times 10^{-4}c$, and the trailing-edge clustering is $2 \times 10^{-3}c$. For multi-element configurations, the H-topology grids contain approximately 31,000 nodes. The off-wall spacing is $2 \times 10^{-6}c$, the distance to the outer boundary is $12c$, the spacing at the grid stagnation points is $2 \times 10^{-5}c$, and the trailing-edge clustering is $2 \times 10^{-3}c$. The reported CPU times are obtained on a 667-MHz Alpha 21264 processor (SPECfp 2000 rating of 562 peak).

Validation

Flow-Solver Performance

A fast solution of the flow equations is a critical component of an effective design algorithm because an evaluation of the objective function is required at each iteration of the optimizer. The performance of the flow solver is examined for the NLR 7301 configuration at $M_\infty = 0.25$, $\alpha = 8$ deg, and $Re = 2.51 \times 10^6$. Figure 3 shows that the Newton–Krylov (NK) flow solver is approximately two to three times faster than the approximate-factorization (AF) flow solver. For many cases, this speedup can be even larger. Initially, the convergence rate of both flow solvers is identical because AF is used as a startup procedure for the NK flow solver.

One of the main difficulties associated with Newton's method is the startup procedure. The NK flow solver is particularly well suited for the design problem because once we obtain the solution for the initial airfoil shape, we warm-start the remaining flow solves. Hence, the flow solution from the current design iteration is used as the initial guess for the next design iteration. If the stepsizes during the line-search procedure are sufficiently small, the startup procedure using approximate factorization is not necessary. The warm-started flow solves typically converge in two-thirds of the original flow solve time.

Accuracy and Efficiency of Gradient Computation

Finite difference gradients provide a benchmark that is used to establish the accuracy of the gradient computation using the adjoint method. A subsonic lift-enhancement problem for the NLR 7301 configuration is considered. During the computation of the finite difference gradient, the flow solution is converged 14 orders of magnitude. The adjoint equation is converged eight orders of magnitude.

The freestream conditions are $M_\infty = 0.25$, $\alpha = 4$ deg, and $Re = 2.51 \times 10^6$. We compute the gradient of the objective function, Eq. (4), with respect to control point 5 on the main airfoil (denoted as 5M), control point 4 on the flap (denoted as 4F), and the horizontal and vertical flap displacements F_x and F_y, respectively (Fig. 1). The target drag coefficient C_D^* is set equal to the initial drag coefficient, whereas the target lift coefficient C_L^* is set equal to 2.2, which represents a 2.5% increase from the initial value. The values of ω_L and ω_D in Eq. (4) are both set to 1.0, and there are no side constraints. Table 1 shows that there is an excellent agreement between the finite-difference and adjoint gradients.

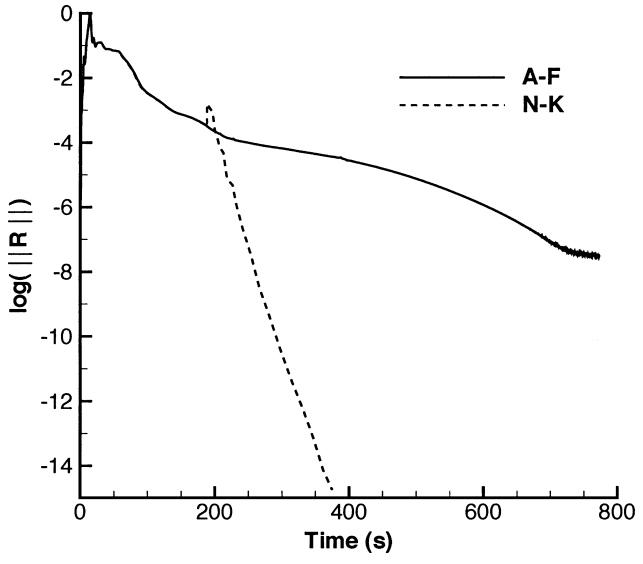

Fig. 3 Flow-solver performance.

Table 1 Gradient accuracy

Design variable	Finite difference	Adjoint, % difference[a]
5M	−0.01228	0.02
4F	−0.08533	−0.19
F_x	−0.02591	0.06
F_y	−0.03363	−0.05

[a] $(\mathcal{G} - \mathcal{G}_{FD})/\mathcal{G}_{FD} \times 100$.

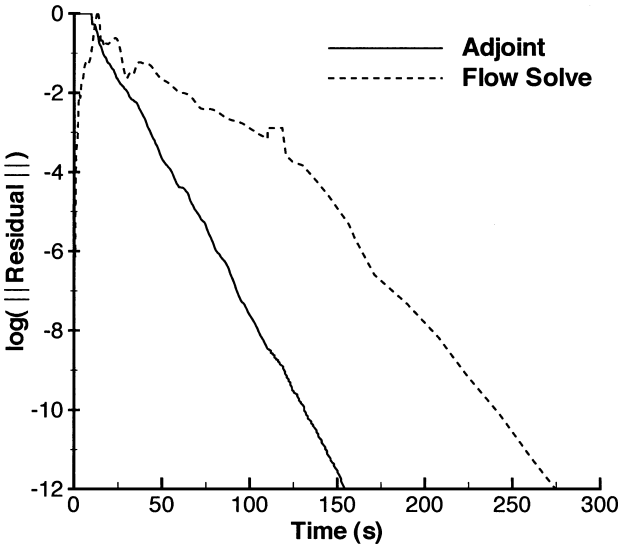

Fig. 4 Comparison of adjoint and flow solve convergence times.

Figure 4 compares the convergence history of the adjoint and flow equations with respect to CPU time. The time for the formation of the preconditioning matrices is included in Fig. 4. (In Fig. 4, the "flat step" in the convergence of the flow solver after a three order-of-magnitude decrease in the residual indicates the formation time of the preconditioner. For the adjoint equation, this time is indicated at the start of the convergence history.) It is necessary to converge the adjoint equation only three orders of magnitude to obtain gradients of sufficient accuracy.[42–44] This level of convergence is achieved in approximately 45 s, as shown in Fig. 4. For the flow equations, we typically reduce the residual by 10 orders of magnitude to prevent stalling of the line searches once the solution is close to the optimum. This convergence level is achieved in 245 s, and consequently, the gradient is obtained in less than one-fifth of the flow solve time.

Design Examples

Optimization of High-Lift Configurations

The first design example demonstrates the performance of the NK algorithm for the optimization of complex high-lift aerodynamic configurations. This optimization is based on a single operating point and objective function, but we consider the issue of local vs global minima. The goal is to determine the optimal gap and overlap distances for the NLR 7301 configuration, such that the modified configuration achieves a higher lift coefficient while maintaining the same (or lower) drag coefficient as the original configuration. The freestream conditions are $M_\infty = 0.25$, $\alpha = 4$ deg, and $Re = 2.51 \times 10^6$. The initial values of C_L and C_D are 2.145 and 0.04720, respectively. The objective function is given by Eq. (4),

Table 2 Gap-overlap optimization summary

Design	C_L	C_D	Gap, $\%c$	Overlap, $\%c$
NLR 7301	2.145	0.04720	2.40	−5.31
1	2.165	0.04687	1.99	−4.28
2	2.173	0.04677	1.95	−3.30
Final	2.175	0.04675	2.02	−2.68
Target	2.180	≤0.0472		

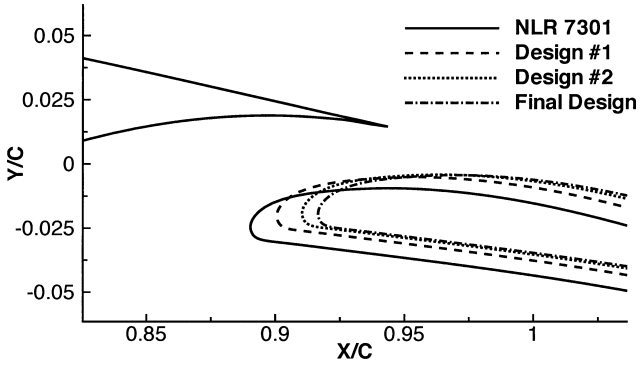

Fig. 5 Flap position summary.

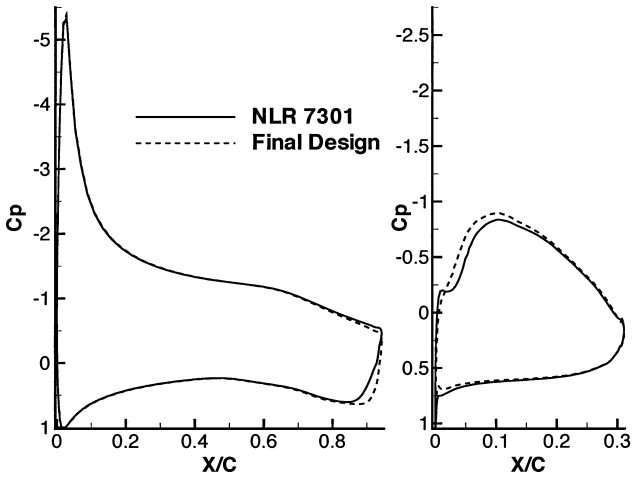

Fig. 6 C_p distribution for main element and flap.

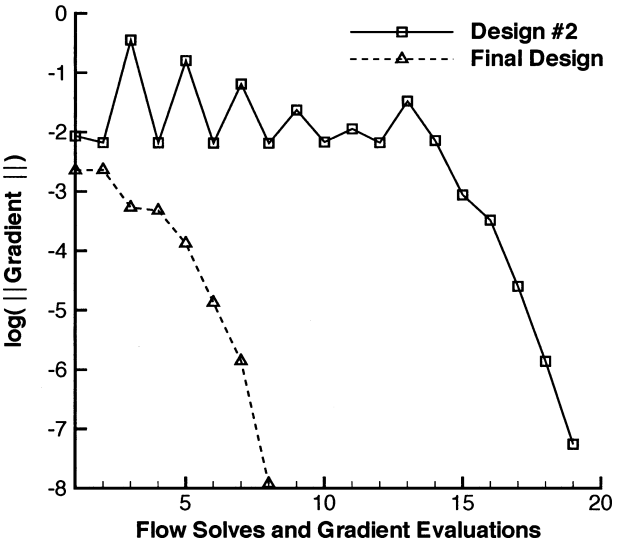

Fig. 7 Convergence histories for gap-overlap optimization.

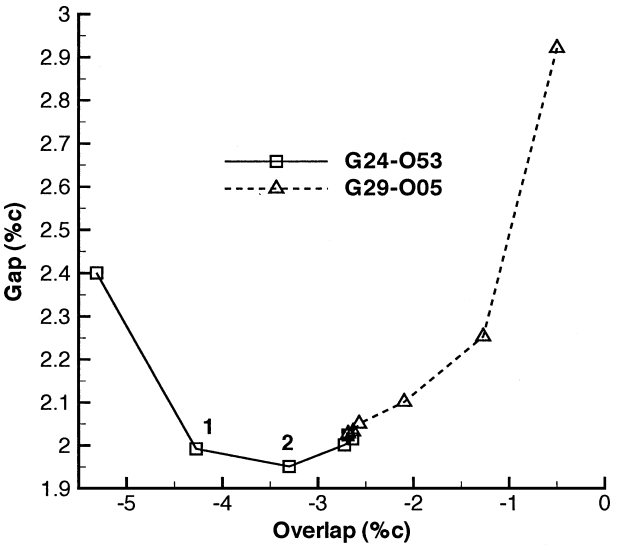

Fig. 8 Convergence to optimal gap-overlap distances from two distinct initial conditions.

where we set $C_L^* = 2.180$ and C_D^* equal to the initial drag coefficient. The weights ω_L and ω_D are set to 1.0. The design variables are the horizontal and vertical displacements of the trailing edge of the flap, as indicated in Fig. 1. The gap and overlap limits are set to $\pm 0.5\%c$ and $\pm 1.0\%c$, respectively, based on the initial configuration. The weight associated with the gap and overlap constraints is set to 0.05.

Table 2 and Fig. 5 summarize the results. Within a few flow and gradient evaluations, the flap reaches the maximum allowable overlap distance of approximately $-4.3\%c$, at which point the overlap penalty function becomes active. The optimization converges to design 1 configuration, shown in Fig. 5. A new grid is generated for this configuration, and the corresponding values of C_L and C_D are given in Table 2. The optimization is restarted from the new grid with the same objective function. This procedure is continued until convergence to the final design is obtained (Fig. 5), where the gap and overlap constraints are no longer active. Note that the drag objective is satisfied for all of the designs. Consequently, the optimization is purely attempting to maximize the lift coefficient. Overall, a 1.4% increase in the value of the lift coefficient is obtained. This is achieved by an increased loading on the main element as well as the flap, as shown in Fig. 6.

Example convergence histories for design 2 and final configurations are shown in Fig. 7. The oscillations in the L_2 norm of the gradient for design 2 are due to the presence of the gap and overlap constraints. The norm of the gradient is reduced by several orders of magnitude, which indicates that the optimization converged to a local minimum. Note that the approximate CPU time for each flow and gradient computation indicated in Fig. 7 is shown in Fig. 4. For additional high-lift design examples using the NK algorithm, see Ref. 45.

Given that the target value of the lift coefficient is not achieved at the final design configuration (Table 2), it is somewhat surprising that further design improvements cannot be realized by further extending the effective chord of the configuration. The convergence of the gradient in Fig. 7 indicates that a local optimum has been found, but a global optimum is not guaranteed. To verify the uniqueness of the optimal solution, the optimization is restarted from a different initial condition. The flap is repositioned to a gap of $2.9\%c$ and an overlap of $-0.5\%c$, that is, the leading edge of the flap is almost aligned with the trailing edge of the main element. Figure 8 shows that the optimization converges to the same optimal solution. The data labeled G24-O53 show the convergence to the optimal solution from the original configuration, with designs 1 and 2 indicated, whereas the data labeled G29-O05 show the convergence to the same optimal solution from the new initial conditions.

Multi-Objective Optimization

The performance of the NK algorithm is presented for the computation of a Pareto front that is based on two competing objective functions. In particular, we consider the design of an airfoil shape to achieve specified lift and drag coefficients using the following two objectives:

$$\mathcal{J}_L = \left(1 - C_L / C_L^*\right)^2 \tag{18}$$

$$\mathcal{J}_D = \left(1 - C_D / C_D^*\right)^2 \tag{19}$$

The target lift and drag coefficients are chosen such that, for a given set of design variables and constraints, the two objectives cannot be satisfied simultaneously. The objectives are competing because a reduction in drag will typically result in a reduction in lift due to the decrease in the thickness and camber of the airfoil. Consequently, this problem does not have a unique solution. Instead, we seek to find a set of noninferior solutions (referred to as a Pareto front) where an improvement in one of the objectives results in a degradation of the other.

There are numerous techniques to solve multi-objective problems.[46,47] The technique used here is the weighted-sum method. The vector of the objective functions is converted to a scalar by assigning a weight to each objective and then forming a sum of the objectives. The resulting objective function is similar to Eq. (8) and is given by

$$\mathcal{J} = \omega_L \mathcal{J}_L + (1 - \omega_L)\mathcal{J}_D + \omega_T \sum_{j=1}^{N_c} C_j \tag{20}$$

where $\omega_T = 1.0$.

The results are presented for the following transonic design example. The freestream conditions are $M_\infty = 0.7$ and $Re = 9 \times 10^6$. We specify a target lift coefficient of 0.55 and a target drag coefficient of 0.0095. The initial airfoil is the NACA 0012 airfoil. The airfoil shape is described with 15 B-spline control points, and we use 10 control points as design variables, as shown in Fig. 9. The angle of attack is also a design variable, resulting in a total of 11 design variables. In addition, we specify three thickness constraints as summarized in Table 3.

The computed Pareto front is shown in Fig. 10, where the tradeoff between the competing objectives is clearly captured. The label TC denotes the thickness-constraint penalty value. Also shown are two sample airfoil shapes obtained at the end-points of the front. Aerodynamic coefficients for a few selected solutions are provided in Table 4.

Table 3 Thickness constraints

TC number	Location, %c	Thickness, %c
1	25.0	11.8
2	92.0	0.9
3	99.0	0.2

Table 4 Aerodynamic coefficients for selected Pareto optimal solutions

ω_L	C_L	C_D	α
0.9	0.5440	0.01204	0.264
0.7	0.5291	0.01187	0.222
0.5	0.5074	0.01169	0.167
0.3	0.4693	0.01145	0.0906
0.1	0.3681	0.01099	−0.0557

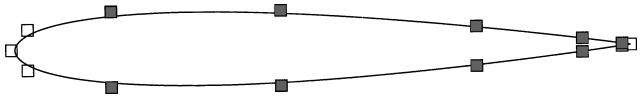

Fig. 9 B-spline control points and design variables (shaded control points) for the NACA 0012 airfoil.

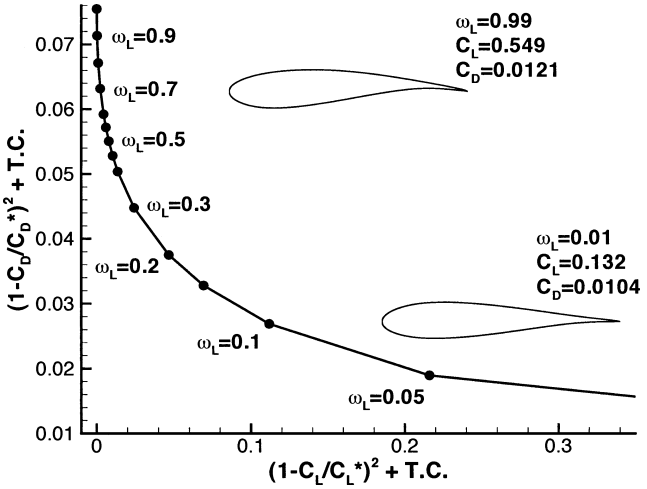

Fig. 10 Pareto front.

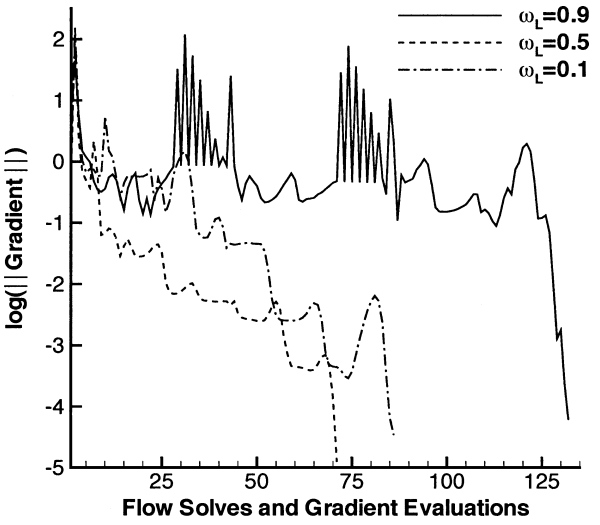

Fig. 11 Gradient convergence histories for selected Pareto front solutions.

To ensure that an optimal solution is attained for each value of ω_L, we require a reduction of at least three orders of magnitude in the L_2 norm of the gradient. Example convergence histories are shown in Fig. 11. The first optimal solution is obtained for $\omega_L = 0.9$, which requires approximately 130 flow and gradient evaluations. The oscillations in the L_2 norm of the gradient are mainly due to the activation of thickness constraints during the line-search procedure. The solutions for the remaining values of ω_L are computed in decreasing order by warm-starting the optimization from the previous solution. The warm-started solutions are typically obtained in 65 to 90 flow and gradient evaluations, as indicated in Fig. 11. An example convergence history of the objective function is shown in Fig. 12 for $\omega_L = 0.9$. The values of the objective function are plotted at the end of each search direction, that is, when the line-search exit criteria are satisfied. Note that, within 25 flow and gradient evaluations, the objective function is converged to engineering accuracy. On average, the CPU times required for each flow and gradient computation are roughly 30 and 9 s, respectively.

Because the Pareto front shown in Fig. 10 has been obtained using a gradient-based method, the convergence to a true, or global, Pareto front is not guaranteed. To investigate whether a global front has been captured, we solve this multi-objective problem using a genetic algorithm developed by Holst and Pulliam.[10] Note that the NK algorithm and the genetic algorithm use identical spatial discretization of the flow equations, objective functions and constraints, as well as design variables.

The results are summarized in Fig. 13, where we show the original, gradient-based front (Gradient; Fig. 13) and a front computed

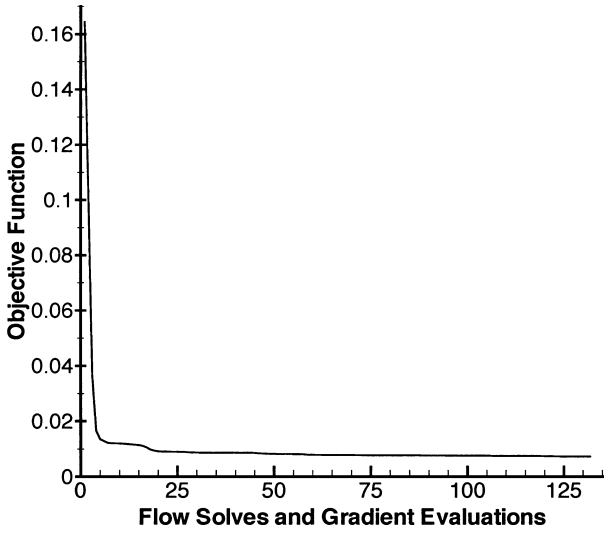

Fig. 12 Objective function convergence history for $\omega_L = 0.9$.

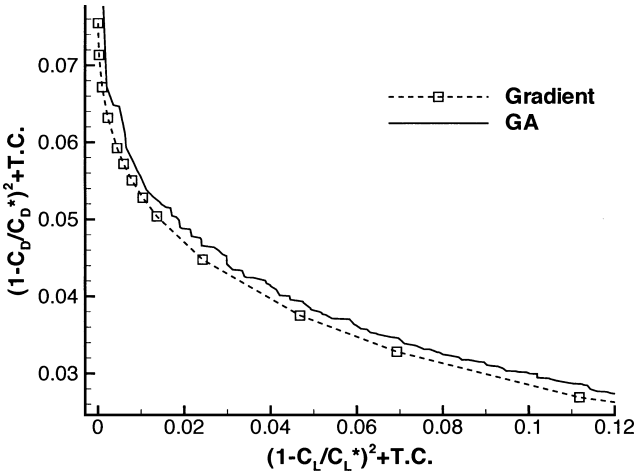

Fig. 13 Comparison of Pareto fronts obtained using the gradient algorithm and GA.

by the genetic algorithm (GA; Fig. 13) using a dominance-based approach.[46] The dominance-based approach is specifically designed to capture global Pareto fronts; however, its computational cost is greater when compared to other techniques. When the GA is used, the Pareto front is obtained in 150 generations, which requires approximately 3000 flow evaluations. Overall, the GA results confirm that the gradient-based front is a global Pareto front. Furthermore, it is well known that GAs exhibit slow convergence rates when close to an optimal solution. This is indicated in Fig. 13, where slightly better results are obtained by the NK algorithm.

Multipoint Optimization

To investigate the performance of the NK algorithm for multipoint optimization problems, the design of a low-drag airfoil for transonic flight conditions at a specified lift coefficient is considered. This example is based on one of the cases studied by Drela.[24] The objective function is given by Eq. (4), where the target drag coefficient C_D^* is set to 0.013, the target lift coefficient C_L^* is set to 0.733, and the Reynolds number is 9.0×10^6. The initial airfoil is the Royal Aircraft Establishment (RAE) 2822 airfoil. The airfoil shape is described with 25 control points, and we use 19 control points as design variables, as well as the angle of attack. The B-spline control points together with the active design variables are shown in Fig. 14. The values of ω_L and ω_D are set to 1.0 and 0.1, respectively. In addition, three airfoil TCs are specified, as summarized in Table 5. The constraint at 35%c represents the initial airfoil thickness, whereas the constraints near the trailing edge are used to prevent airfoil surface crossover. The value of ω_T is set to 1.0.

Table 5 Thickness constraints

TC number	Location, %c	Thickness, %c
1	35.0	12.04
2	96.0	0.5
3	99.0	0.12

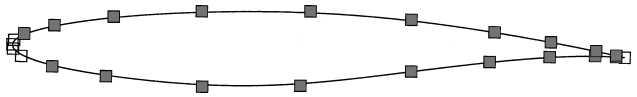

Fig. 14 B-spline control points and design variables (shaded control points) for the RAE 2822 airfoil.

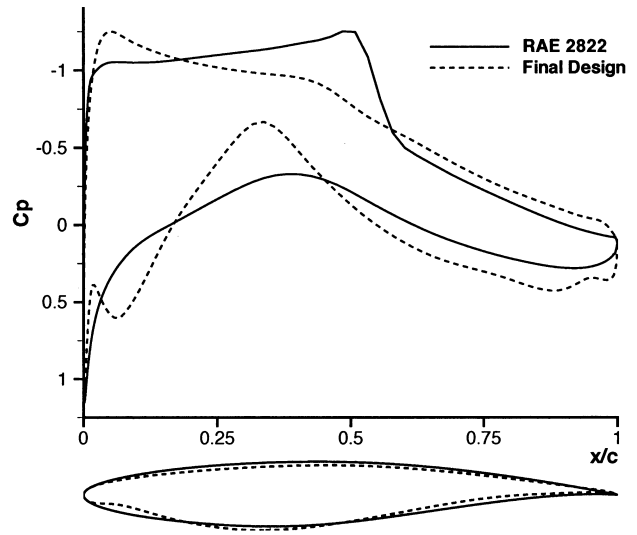

a) Pressure distribution and airfoil shapes ($M = 0.74$)

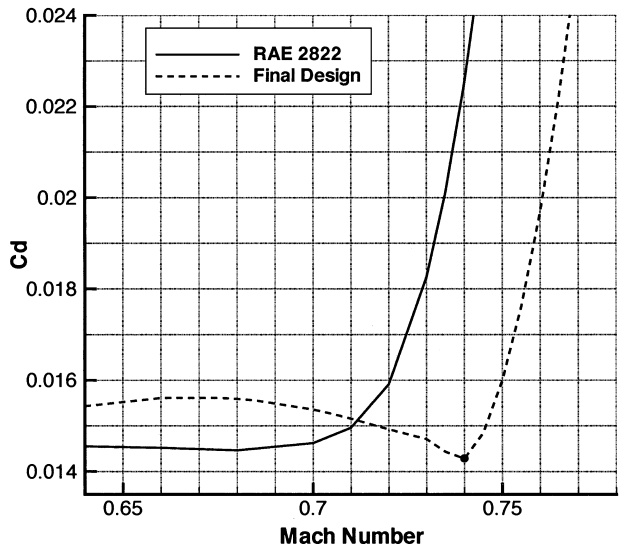

b) Drag coefficient at $C_L = 0.733$

Fig. 15 Single-point optimization.

First, we consider a single-point optimization problem for the design Mach number of 0.74. Figure 15a shows the initial and final pressure distributions and the corresponding airfoil shapes. Figure 15b shows the values of the drag coefficient over a range of Mach numbers for $C_L = 0.733$. The drag coefficient is reduced by 36.4% at the design Mach number. The final thickness at 35%c is 12.0%c,

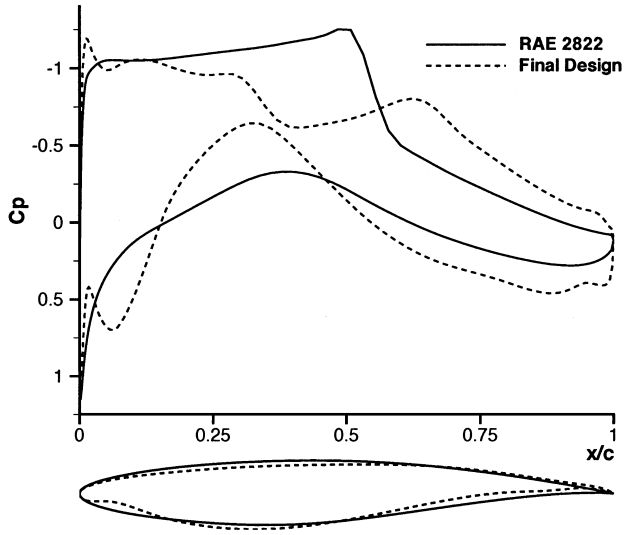

a) Pressure distribution and airfoil shapes ($M = 0.74$)

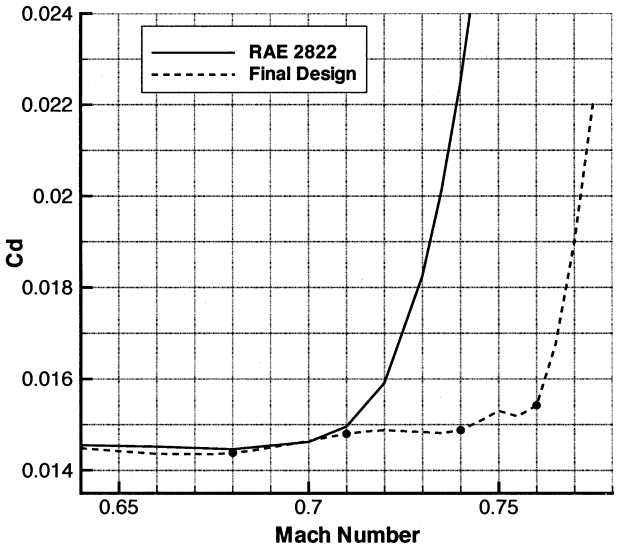

b) Drag coefficient at $C_L = 0.733$

Fig. 16 Four-point optimization.

which is very close to the desired thickness. However, for Mach numbers below 0.71, the optimized airfoil performs significantly worse than the original airfoil.

Next, we consider a four-point optimization problem, where the design Mach numbers are 0.68, 0.71, 0.74, and 0.76. The weights assigned to each design Mach number for the weighted-sum method, Eq. (5), are 1.0, 1.0, 2.0, and 3.0, respectively. Figure 16a shows the initial and final pressure distributions and the corresponding airfoil shapes for the design point $M = 0.74$. Figure 16b shows the values of the drag coefficient over a range of Mach numbers for $C_L = 0.733$. When compared with the initial RAE 2822 airfoil, the new design achieves significantly lower drag values for Mach numbers above 0.71. The drag-divergence Mach number is increased by 7.0%. The drag coefficient is reduced by 33.8% at $M = 0.74$, which is only slightly less than the reduction obtained for the single-point optimization problem. Although the resulting airfoil is not suitable for practical use, with judicious definition of objectives and constraints for a specific application, the NK algorithm can provide realistic designs.

Conclusions

An NK algorithm for the design of single- and multi-element airfoil configurations has been presented. The accuracy of the objective function gradient, based on the discrete-adjoint method, is excellent. Furthermore, the gradient is obtained in approximately one-third to one-fifth of the flow solve time. The design examples demonstrate that the new algorithm provides an effective approach for aerodynamic design problems with multiple objectives and operating points. Future work should concentrate on more detailed comparisons between the gradient-based algorithms and GAs for complex multi-objective problems. In addition, the capabilities of the new algorithm need to be investigated for practical three-dimensional design problems with more complex objectives and constraints (preferably defined by industry experts).

Acknowledgments

This research was supported by the Natural Sciences and Engineering Research Council of Canada, as well as Bombardier Aerospace, Pratt and Whitney Canada, and an Ontario Graduate Scholarship from the Government of Ontario. The authors gratefully acknowledge Samy Elias for his assistance with the multipoint design cases.

References

[1]Rumsey, C. L., and Ying, S. X., "Prediction of High Lift: Review of Present CFD Capability," *Progress in Aerospace Sciences*, Vol. 38, No. 2, 2002, pp. 145–180.

[2]Jameson, A., Pierce, N. A., and Martinelli, L., "Optimum Aerodynamic Design Using the Navier–Stokes Equations," *Theoretical and Computational Fluid Dynamics*, Vol. 10, No. 1, 1998, pp. 213–237.

[3]Soemarwoto, B. I., and Labrujère, T. E., "Airfoil Design and Optimization Methods: Recent Progress at NLR," *International Journal for Numerical Methods in Fluids*, Vol. 30, No. 2, 1999, pp. 217–228.

[4]Anderson, W. K., and Bonhaus, D. L., "Airfoil Design on Unstructured Grids for Turbulent Flows," *AIAA Journal*, Vol. 37, No. 2, 1999, pp. 185–191.

[5]Nielsen, E. J., and Anderson, W. K., "Aerodynamic Design Optimization on Unstructured Meshes Using the Navier–Stokes Equations," *AIAA Journal*, Vol. 37, No. 11, 1999, pp. 1411–1419.

[6]Kim, C. S., Kim, C., and Rho, O. H., "Sensitivity Analysis for the Navier–Stokes Equations with Two-Equation Turbulence Models," *AIAA Journal*, Vol. 39, No. 5, 2001, pp. 838–845.

[7]Giles, M. B., Duta, M. C., and Müller, J.-D., "Adjoint Code Developments Using the Exact Discrete Approach," AIAA Paper 2001-2596, June 2001.

[8]Obayashi, S., "Aerodynamic Optimization with Evolutionary Algorithms," *Inverse Design and Optimization Methods, Lecture Series 1997-05*, edited by R. A. V. den Braembussche and M. Manna, von Kármán Inst. for Fluid Dynamics, Brussels, 1997.

[9]Giannakoglou, K. C., "Design of Optimal Aerodynamic Shapes Using Stochastic Optimization Methods and Computational Intelligence," *Progress in Aerospace Sciences*, Vol. 38, No. 1, 2002, pp. 43–76.

[10]Holst, T. L., and Pulliam, T. H., "Aerodynamic Shape Optimization Using a Real-Number-Encoded Genetic Algorithm," AIAA Paper 2001-2473, June 2001.

[11]Hicks, R. M., Murman, E. M., and Vanderplaats, G. N., "An Assessment of Airfoil Design by Numerical Optimization," NASA TM X-3092, July 1974.

[12]Elliott, J., and Peraire, J., "Constrained, Multipoint Shape Optimisation for Complex 3D Configurations," *Aeronautical Journal*, Vol. 102, No. 1017, 1998, pp. 365–376.

[13]Tse, D., and Chan, L., "Transonic Airfoil Design Optimization Using Soft Computing Methods," *Canadian Aeronautics and Space Journal*, Vol. 46, No. 2, 2000, pp. 65–73.

[14]Reuther, J. J., Alonso, J. J., Rimlinger, M. J., and Jameson, A., "Aerodynamic Shape Optimization of Supersonic Aircraft Configurations via an Adjoint Formulation on Distributed Memory Parallel Computers," *Computers and Fluids*, Vol. 28, 1999, pp. 675–700.

[15]Nadarajah, S. K., Jameson, A., and Alonso, J. J., "An Adjoint Method for the Calculation of Remote Sensitivities in Supersonic Flow," AIAA Paper 2002-0261, Jan. 2002.

[16]Eyi, S., Lee, K. D., Rogers, S. E., and Kwak, D., "High-Lift Design Optimization Using Navier–Stokes Equations," *Journal of Aircraft*, Vol. 33, No. 3, 1996, pp. 499–504.

[17]Greenman, R. M., "Two-Dimensional High-Lift Optimization Using Neural Networks," NASA TM-1998-112233, June 1998.

[18]Alexandrov, N. M., Nielsen, E. J., Lewis, R. M., and Anderson, W. K., "First-Order Model Management with Variable-Fidelity Physics Applied to Multi-Element Airfoil Optimization," AIAA Paper 2000-4886, Sept. 2000.

[19]Nielsen, E. J., and Anderson, W. K., "Recent Improvements in Aerodynamic Design Optimization on Unstructured Meshes," *AIAA Journal*, Vol. 40, No. 6, 2002, pp. 1155–1163.

[20]Kim, S., Alonso, J. J., and Jameson, A., "Design Optimization of High-Lift Configurations Using a Viscous Continuous Adjoint Method," AIAA Paper 2002-0844, Jan. 2002.

[21]Nemec, M., and Zingg, D. W., "From Analysis to Design of High-Lift Configurations Using a Newton–Krylov Algorithm," International Council of the Aeronautical Sciences, ICAS Paper 173, Sept. 2002.

[22]van Dam, C. P., "The Aerodynamic Design of Multi-Element High-Lift Systems for Transport Airplanes," *Progress in Aerospace Sciences*, Vol. 38, No. 2, 2002, pp. 101–144.

[23]Martins, J. R. R. A., Alonso, J. J., and Reuther, J. J., "High-Fidelity Aero-Structural Design Optimization of a Supersonic Business Jet," AIAA Paper 2002-1483, April 2002.

[24]Drela, M., "Pros & Cons of Airfoil Optimization," *Frontiers of Computational Fluid Dynamics 1998*, edited by D. A. Caughey and M. M. Hafez, World Scientific, Singapore, 1998, pp. 363–381.

[25]Li, W., Huyse, L., and Padula, S., "Robust Airfoil Optimization to Achieve Drag Reduction over a Range of Mach Numbers," *Structural and Multidisciplinary Optimization*, Vol. 24, No. 1, 2002, pp. 38–50.

[26]Huyse, L., Padula, S., Lewis, R. M., and Li, W., "Probabilistic Approach to Free-Form Airfoil Shape Optimization Under Uncertainty," *AIAA Journal*, Vol. 40, No. 9, 2002, pp. 1764–1772.

[27]Nemec, M., and Zingg, D. W., "Newton–Krylov Algorithm for Aerodynamic Design Using the Navier–Stokes Equations," *AIAA Journal*, Vol. 40, No. 6, 2002, pp. 1146–1154.

[28]Saad, Y., and Schultz, M. H., "GMRES: A Generalized Minimal Residual Algorithm for Solving Nonsymmetric Linear Systems," *SIAM Journal on Scientific and Statistical Computing*, Vol. 7, No. 3, 1986, pp. 856–869.

[29]Farin, G. E., *Curves and Surfaces for Computer-Aided Geometric Design: A Practical Guide*, 4th ed., Academic Press, San Diego, CA, 1997.

[30]Van Den Berg, B., "Boundary Layer Measurements on a Two-Dimensional Wing with Flap," National Aerospace Lab., NLR TR 79009 U, Amsterdam, Jan. 1979.

[31]Pulliam, T. H., "Efficient Solution Methods for the Navier–Stokes Equations," Technical Rept., Lecture Notes for the von Kármán Inst. for Fluid Dynamics Lecture Series: Numerical Techniques for Viscous Flow Computation in Turbomachinery Bladings, Brussels, Jan. 1986.

[32]Spalart, P. R., and Allmaras, S. R., "A One-Equation Turbulence Model for Aerodynamic Flows," AIAA Paper 92-0439, Jan. 1992.

[33]Nocedal, J., and Wright, S. J., *Numerical Optimization*, Springer-Verlag, New York, 1999.

[34]Nelson, T. E., Zingg, D. W., and Johnston, G. W., "Compressible Navier–Stokes Computations of Multielement Airfoil Flows Using Multiblock Grids," *AIAA Journal*, Vol. 32, No. 3, 1994, pp. 506–511.

[35]Godin, P., Zingg, D. W., and Nelson, T. E., "High-Lift Aerodynamic Computations with One- and Two-Equation Turbulence Models," *AIAA Journal*, Vol. 35, No. 2, 1997, pp. 237–243.

[36]Pueyo, A., and Zingg, D. W., "Efficient Newton–Krylov Solver for Aerodynamic Computations," *AIAA Journal*, Vol. 36, No. 11, 1998, pp. 1991–1997.

[37]Nemec, M., "Optimal Shape Design of Aerodynamic Configurations: A Newton–Krylov Approach," Ph.D. Dissertation, Inst. for Aerospace Studies, Univ. of Toronto, Toronto, June 2003; also URL: http://oddjob.utias.utoronto.ca/marian/.

[38]Chow, E., and Saad, Y., "Experimental Study of ILU Preconditioners for Indefinite Matrices," *Journal of Computational and Applied Mathematics*, Vol. 86, 1997, pp. 387–414.

[39]Gunzburger, M. D., "Introduction into Mathematical Aspects of Flow Control and Optimization," *Inverse Design and Optimization Methods*, Vol. 1997–05, von Kármán Inst. for Fluid Dynamics, Brussels, 1997, pp. 1–20.

[40]Giles, M. B., and Pierce, N. A., "An Introduction to the Adjoint Approach to Design," *Flow, Turbulence and Combustion*, Vol. 65, No. 3/4, 2000, pp. 393–415.

[41]Giles, M. B., and Pierce, N. A., "Analytic Adjoint Solutions for the Quasi-One-Dimensional Euler Equations," *Journal of Fluid Mechanics*, Vol. 426, 2001, pp. 327–345.

[42]Reuther, J. J., Jameson, A., Alonso, J. J., Rimlinger, M. J., and Saunders, D., "Constrained Multipoint Aerodynamic Shape Optimization Using an Adjoint Formulation and Parallel Computers, Part 2," *Journal of Aircraft*, Vol. 36, No. 1, 1999, pp. 61–74.

[43]Nielsen, E. J., "Aerodynamic Design Sensitivities on an Unstructured Mesh Using the Navier–Stokes Equations and a Discrete Adjoint Formulation," Ph.D. Dissertation, Dept. of Aerospace Engineering, Virginia Polytechnic Inst. and State Univ., Blacksburg, VA, Dec. 1998.

[44]Kim, H.-J., Sasaki, D., Obayashi, S., and Nakahashi, K., "Aerodynamic Optimization of Supersonic Transport Wing Using Unstructured Adjoint Method," *AIAA Journal*, Vol. 39, No. 6, 2001, pp. 1011–1020.

[45]Nemec, M., and Zingg, D. W., "Optimization of High–Lift Configurations Using a Newton–Krylov Algorithm," AIAA Paper 2003-3957, June 2003.

[46]Coello, C. A. C., "A Comprehensive Survey of Evolutionary-Based Multiobjective Optimization Techniques," *Knowledge and Information Systems*, Vol. 1, No. 3, 1999, pp. 269–308.

[47]Marco, N., Désidéri, J.-A., and Lanteri, S., "Multi-Objective Optimization in CFD by Genetic Algorithms," INRIA Technical Rept. 3686, Inst. National de Recherche en Informatique et en Automatique, Sophia Antipolis Cedex, France, April 1999.

E. Livne
Associate Editor